UC Irvine
UC Irvine Previously Published Works

Title

Effect of climate change on surface ozone over North America, Europe, and East Asia

Permalink

Journal

ISSN

Authors

Schnell, Jordan L
Prather, Michael J
Josse, Beatrice
et al.

Publication Date

DOI

Peer reviewed

Key Points:
- Climate change increases surface ozone in polluted regions and decreases surface ozone in nearby and cleaner regions
- Surface ozone increases are largest at high percentiles even with constant biogenic emissions
- Air quality extremes become more hazardous under future climate warming

Effect of climate change on surface ozone over North America, Europe, and East Asia

Jordan L. Schnell[1], Michael J. Prather[1], Beatrice Josse[2], Vaishali Naik[3], Larry W. Horowitz[4], Guang Zeng[5], Drew T. Shindell[6], and Greg Faluvegi[7]

[1]Department of Earth System Science, University of California, Irvine, California, USA, [2]GAME/CNRM, Météo-France, CNRS–Centre National de Recherches Météorologiques, Toulouse, France, [3]UCAR/NOAA Geophysical Fluid Dynamics Laboratory, National Oceanic and Atmospheric Administration, Princeton, New Jersey, USA, [4]Geophysical Fluid Dynamics Laboratory, National Oceanic and Atmospheric Administration, Princeton, New Jersey, USA, [5]National Institute of Water and Atmospheric Research, Lauder, New Zealand, [6]Nicholas School of the Environment, Duke University, Durham, North Carolina, USA, [7]NASA Goddard Institute for Space Studies and Columbia Earth Institute, Columbia University, New York, New York, USA

Abstract The effect of future climate change on surface ozone over North America, Europe, and East Asia is evaluated using present-day (2000s) and future (2100s) hourly surface ozone simulated by four global models. Future climate follows RCP8.5, while methane and anthropogenic ozone precursors are fixed at year 2000 levels. Climate change shifts the seasonal surface ozone peak to earlier in the year and increases the amplitude of the annual cycle. Increases in mean summertime and high-percentile ozone are generally found in polluted environments, while decreases are found in clean environments. We propose that climate change augments the efficiency of precursor emissions to generate surface ozone in polluted regions, thus reducing precursor export to neighboring downwind locations. Even with constant biogenic emissions, climate change causes the largest ozone increases at high percentiles. In most cases, air quality extreme episodes become larger and contain higher ozone levels relative to the rest of the distribution.

1. Introduction

Future surface ozone (O_3) will be determined by multiple factors, including changes in stratosphere-troposphere exchange [e.g., *Zeng and Pyle*, 2003], changes in anthropogenic and natural emissions of O_3 precursors, plus climate-induced shifts in meteorology and background tropospheric chemistry [*Jacob and Winner*, 2009; *Fiore et al.*, 2012, 2015]. Future scenarios of O_3 precursors adopted in the Fifth Assessment Report of the Intergovernmental Panel on Climate Change (IPCC AR5) [*Cubasch et al.*, 2013; *Kirtman et al.*, 2013; *Myhre et al.*, 2013] project lower overall anthropogenic emissions by 2100 in most locations, but one scenario has large increases in methane (also an O_3 precursor). Future air quality is expected to improve over North America and Europe in all scenarios and improve worldwide if methane increases are avoided [e.g., *Kirtman et al.*, 2013; *Pfister et al.*, 2014]. These IPCC results combine climate and emission changes. Climate change in and of itself will likely reduce O_3 in unpolluted conditions [*Johnson et al.*, 1999] but possibly increase surface O_3 in polluted regions (e.g., "climate change penalty" of *Wu et al.* [2008]), thus offsetting the benefits of precursor emission reductions. Here we examine the role of climate change on continental surface O_3 using global chemistry model simulations with fixed anthropogenic emissions of ozone precursors (and fixed methane abundances) as climate changes from 2000 to 2100.

Climate change will affect surface O_3 through numerous temperature-driven pathways [e.g., *Jacob and Winner*, 2009; *Thambiran and Diab*, 2010; *Fiore et al.*, 2012]. While these pathways have a physical basis, the magnitude is usually derived from present-day correlations with observed surface O_3 and meteorological proxy variables meant to represent the pathway [e.g., *Ordonez et al.*, 2005; *Camalier et al.*, 2007]. Fully coupled chemistry-climate model simulations on the time-space scales relevant for air quality studies are uncommon, so future O_3 changes are often statistically downscaled using proxy data, i.e., global or regional climate model projections of relevant meteorological variables [e.g., *Mahmud et al.*, 2008; *Holloway et al.*, 2008]. Unfortunately, these O_3 meteorology correlations may not apply to future climate since they often reflect a common underlying driver and do not represent the net effect of photochemistry, meteorology, and land-atmosphere interactions on O_3 [*Fiore et al.*, 2015]. For example, large O_3 increases often occur during periods with clear skies, high temperatures, and light winds (i.e., stagnation events), which allow for increased O_3 production and accumulation of nearby emissions [*Logan*, 1989; *Hogrefe et al.*, 2004; *Mickley et al.*, 2004;

Leibensperger et al., 2008]. Thus, one can define a stagnation index based on year 2000 meteorology and argue that a year 2100 increase in this index implies a proportionate increase in the worst pollution days [*Horton et al.*, 2014]. However, a stagnation index is just that, a proxy index, and requires that the underlying processes responsible for the present-day correlations be maintained in the future.

Our approach uses hourly surface O_3 simulated by models participating in the Atmospheric Chemistry and Climate Model Intercomparison Project (ACCMIP) conducted in support of the IPCC AR5 [*Lamarque et al.*, 2013; *Naik et al.*, 2013; *Stevenson et al.*, 2013; *Voulgarakis et al.*, 2013; *Young et al.*, 2013]. Other direct studies are generally either limited to a single model, restricted regions, or relied on annual and seasonal average diagnostics [e.g., *Doherty et al.*, 2013; *Clifton et al.*, 2014; *Rieder et al.*, 2015]. We use hourly O_3 to identify the daily and synoptic variability and air quality extremes (AQX), enabling an investigation of climate-driven changes in pollution episodes at high temporal resolution.

2. Data and Domains

2.1. ACCMIP Models

We analyze model results from two ACCMIP experiments: *acchist* (a present-day climatology, henceforth CL2000) and *Em2000Cl2100* (present-day O_3 precursors with year 2100 climate, henceforth CL2100). The ACCMIP models that correctly implemented the experiments and saved hourly surface O_3 are used here: MOCAGE, GFDL-AM3, UM-CAM, and GISS-E2-R (see Table S1 in the supporting information) [*Lamarque et al.*, 2013, and references therein]. Climate change follows the IPCC AR5 high-CO_2 scenario (RCP8.5) with global mean CL2000 to CL2100 surface temperature increases of ~4°C. These two simulations isolate the effects of climate change by fixing anthropogenic emissions of O_3 and aerosol precursors and the methane abundances used for chemistry to present-day levels while forcing the physical climate (and some natural precursor emissions; see below) by RCP8.5 sea surface temperatures and sea ice distributions. *Schnell et al.* [2015] (hereinafter S2015) evaluated the models' present-day surface O_3 climatologies against North American and European observations. Although generally biased high in surface O_3, the models capture the shape and amplitude of the diurnal and annual cycles, large-scale percentile patterns, and the size distribution of AQX episodes. The analysis of S2015 thus provides some confidence in the modeled future changes (see S2015 for a full description of the metrics used here).

While anthropogenic emissions in the ACCMIP were specified, natural emissions were not, so the models used different formula for natural emissions with differing responses to climate changes [*Young et al.*, 2013]. For example, lightning NO_x emissions are usually parameterized as a function of deep convection and hence are climate sensitive. Across our four models, these emissions ranged from 4.4 to 7.7 Tg N a^{-1} for CL2000 and increased by 21% to 44% for CL2100 [*Lamarque et al.*, 2013]. Climate-driven biogenic volatile organic compound (BVOC) emission changes may be responsible for O_3 changes in some regions [*Lin et al.*, 2008]. Isoprene, the most abundant BVOC, is chemically very reactive, either increasing or decreasing near-surface O_3 under high or low NO_x conditions, respectively. Only GISS-E2-R incorporates climate-driven isoprene emissions that increase with increasing temperature [*Guenther et al.*, 1995], and thus, CL2100 has greater (natural) BVOC emissions than CL2000 [*Young et al.*, 2013]. Other direct climate-sensitive feedbacks from increased CO_2 include inhibited isoprene emissions [*Heald et al.*, 2009] or reduced stomatal uptake of O_3 [*Ainsworth and Rogers*, 2007], but neither were included here.

Each model's hourly surface O_3 abundances (typically at 2°–3°) are remapped to a common 1° × 1° grid using first-order conservative mapping to facilitate a more direct intermodel comparison and maintain consistency with S2015. Maximum daily 8 h averages (MDA8) are calculated from the hourly O_3 abundances after adjusting to local solar time. All analyses shown here are performed using the MDA8.

2.2. Domains and Regions

We investigate changes over three continental-scale domains: North America (NA) bounded by 25°N–49°N and 125°W–67°W, Europe (EU) bounded by 36°N–71°N and 11°W–34°E, and East Asia (EA) bounded by 8° N–42°N and 69°E–130°E. Due to differing chemical and climatic regimes, we split each domain into two regions: NA into western (WNA) and eastern (ENA) regions at 96°W, EU into southern (SEU) and northern (NEU) regions at 53°N, and EA into southern (SEA) and northern (NEA) regions at 30°N. The split location for each domain is somewhat arbitrary but roughly divides the domains in half and coincides with natural

breaks in the seasonal chemical regime. Henceforth, the terms "domain" and "region" are used to describe the whole and split domains, respectively.

3. Results

We evaluate 21st century climate-driven changes from decadal differences ($\Delta \equiv$ CL2100 minus CL2000) in the probability distribution (PD) of MDA8 surface O_3 to identify the full scope of changes, from the cleanest to most polluted conditions. At each grid cell and simulated period, we compute seasonal averages as well as percentiles from the daily values. From the multiyear PDs, we calculate seasonal medians as the percentile of the median day in each season. If the seasons were alike, then all would have a percentile ranking of 50%. Regional average changes are calculated as the area-weighted average of the derived changes in all encompassed grid cells. Climate-driven Δ changes are presented in order of increasing percentile, from the low O_3 of boreal winter to the high O_3 of summer.

3.1. Changes in Incoming Boundary and Low-Percentile O_3

Boundary O_3 is defined here as the statistically cleanest air impinging on the continents, providing the baseline O_3 upon which pollution accumulates. For our six continental regions, boundary O_3 largely originates from the marine boundary layer. Modeled surface O_3 changes over adjacent ocean basins are presented in Figure S1 for mean winter (December-January-February, DJF) and Figure S2 for mean summer (June-July-August, JJA). These seasonal average changes should reflect the most basic hemispheric-scale, climate-driven shifts such as increased water vapor.

Over the tropical and subtropical oceans, photochemistry drives a net O_3 loss of ~10%/d, which increases with temperature and water vapor [*Johnson et al.*, 1999], thus enhancing loss in the CL2100 simulation. From Figure S1, all models except MOCAGE show positive ΔDJF (+1 to +5 ppb) over the Pacific and Atlantic Oceans north of ~20°N and a sharp transition to negative ΔDJF (−1 to −8 ppb) to the south. This ΔDJF edge over the Pacific (and Atlantic to a lesser extent) augments the north-south gradient of CL2000 DJF O_3 (not shown). All models show negative ΔDJF over the Indian Ocean adjacent to SEA. We find negative ΔJJA (Figure S2) over all three oceans (except GISS-E2-R over the Pacific and Atlantic). Negative Δ changes are easily attributable to enhanced destruction in a warmer, wetter marine boundary layer. A cause for positive ΔDJF in the extratropics is less clear but may be due to enhanced vertical mixing with high O_3 in the free troposphere or possibly enhanced wintertime photochemical production (e.g., from increased lightning NO_x). Nevertheless, all models except MOCAGE show increased DJF boundary O_3 everywhere except SEA, and all models except GISS-E2-R show decreased JJA boundary O_3.

Figure 1 summarizes percentile and seasonal MDA8 O_3 changes for the four models over six continental regions (i.e., 24 model regions). The colored bars show each model region's MDA8 O_3 Δ change averaged over 10 equal percentile bins (a uniform color means that the entire PD has shifted, whereas red at the high end and blue at the low end mean that the worst days became more polluted and the best days became cleaner). The median percentile of each season's day is shown for CL2000 (black filled markers) and for CL2100 (color filled markers), where the fill color identifies the Δ change in the season's average. Observed CL2000 (S2015) seasonal medians are given for NA and EU regions. The dashed lines at the 13th and 87th percentiles respectively represent the minimum and maximum possible values for a seasonal median (i.e., if all days in a season have the lowest or highest abundances in the entire period).

Modeled CL2000 seasonal percentiles agree with present-day observations over NA and EU in that fall (September-October-November, SON) or winter (DJF) typically has the lowest O_3 percentiles (Figure 1) (see also S2015). Because ΔDJF (and ΔSON, not shown) is positive over the midlatitude oceans, we expect ΔDJF and ΔSON to be positive and they are 0 to +5 ppb for 16 of 24 model regions. Changes in the lowest 10% (Δ5th), however, do not follow these patterns but show decreases (−1 to −4 ppb for 16 of 24 model regions). This pattern fits across models, including UM-CAM with the lowest DJF percentiles, and likely reflects increased daily variability of low-season O_3 in CL2100 (Table S2). For subtropical SEA, we expect Δ5th to be related to ΔJJA when monsoons and tropical, low-O_3 air occurs. Indeed, all models show both negative Δ5th and ΔJJA over SEA, consistent with their negative ΔJJA over the Indian Ocean. These Δ changes in monsoonal surface O_3 could be attributed to enhanced photochemical loss, alterations to the location or intensity of the Asian monsoon [*Christensen et al.*, 2013], or both.
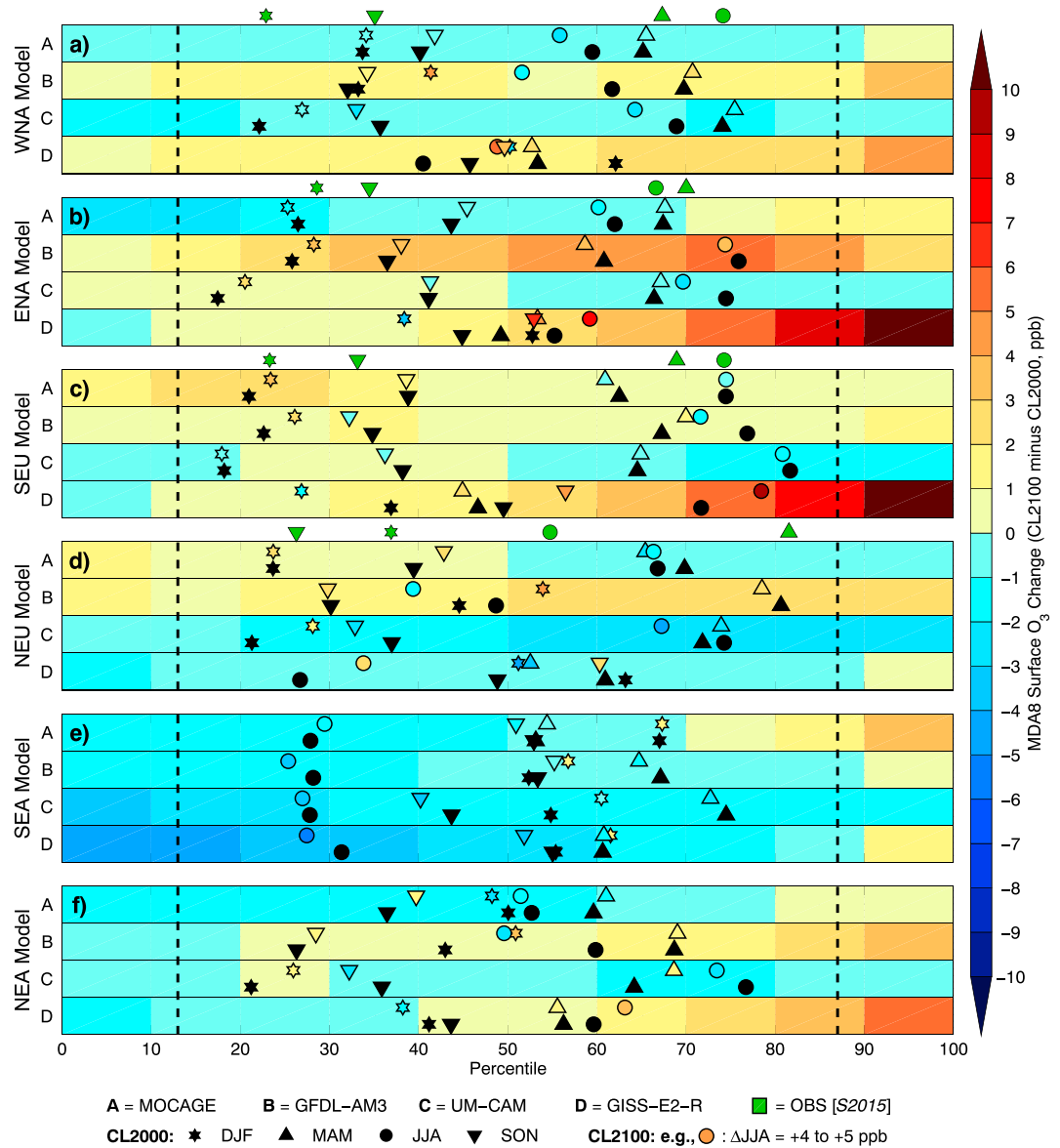
Figure 1. Percentile and seasonal MDA8 surface O$_3$ changes (CL2100 minus CL2000, ppb) for the ACCMIP models MOCAGE (A), GFDL-AM3 (B), UM-CAM (C), and GISS-E2-R (D) over (a) WNA, (b) ENA, (c) SEU, (d) NEU, (e) SEA, and (f) NEA. Colored bars show the absolute MDA8 surface O$_3$ change averaged over 10 equal percentile bins. The median percentiles of the days in winter (DJF), spring (MAM), summer (JJA), and fall (SON) are shown for modeled CL2000 (black markers) and CL2100 (colored markers), where the CL2100 fill colors correspond to the change in each season's average. Observed CL2000 median seasonal percentiles (S2015) are plotted on the top edge of NA and EU regions' subplots (green markers). All changes correspond to the single color bar. Dashed lines at the 13th and 87th percentiles respectively represent the minimum and maximum possible values for a median season percentile.

The geographic patterns of the multimodel mean of Δ5th and ΔDJF are shown in Figures 2a–2c and 2d–2f, respectively, with individual model-domain maps in Figures S3 and S4 and model region averages in Table S2. Consistent with Figure 1, Δ5th is predominately negative and ΔDJF is positive, with some similarity in their geographic patterns. One standout feature in NA ΔDJF is the break at 40°N with positive ΔDJF to the south and negative to the north. The cause may be photochemical with warmer temperatures in the south but is more likely due to circulation changes. Clear differences between Δ5th and ΔDJF for NA and EU occur in areas most influenced by clean maritime air (negative Δ5th and positive ΔDJF), but this is less obvious for EA. Thus, in maritime regions, ΔDJF is driven by CL2100 increases in maritime DJF O$_3$, and extreme low-O$_3$ events (Δ5th) have shifted seasons, generally out of DJF and into JJA or SON (Figure S5).
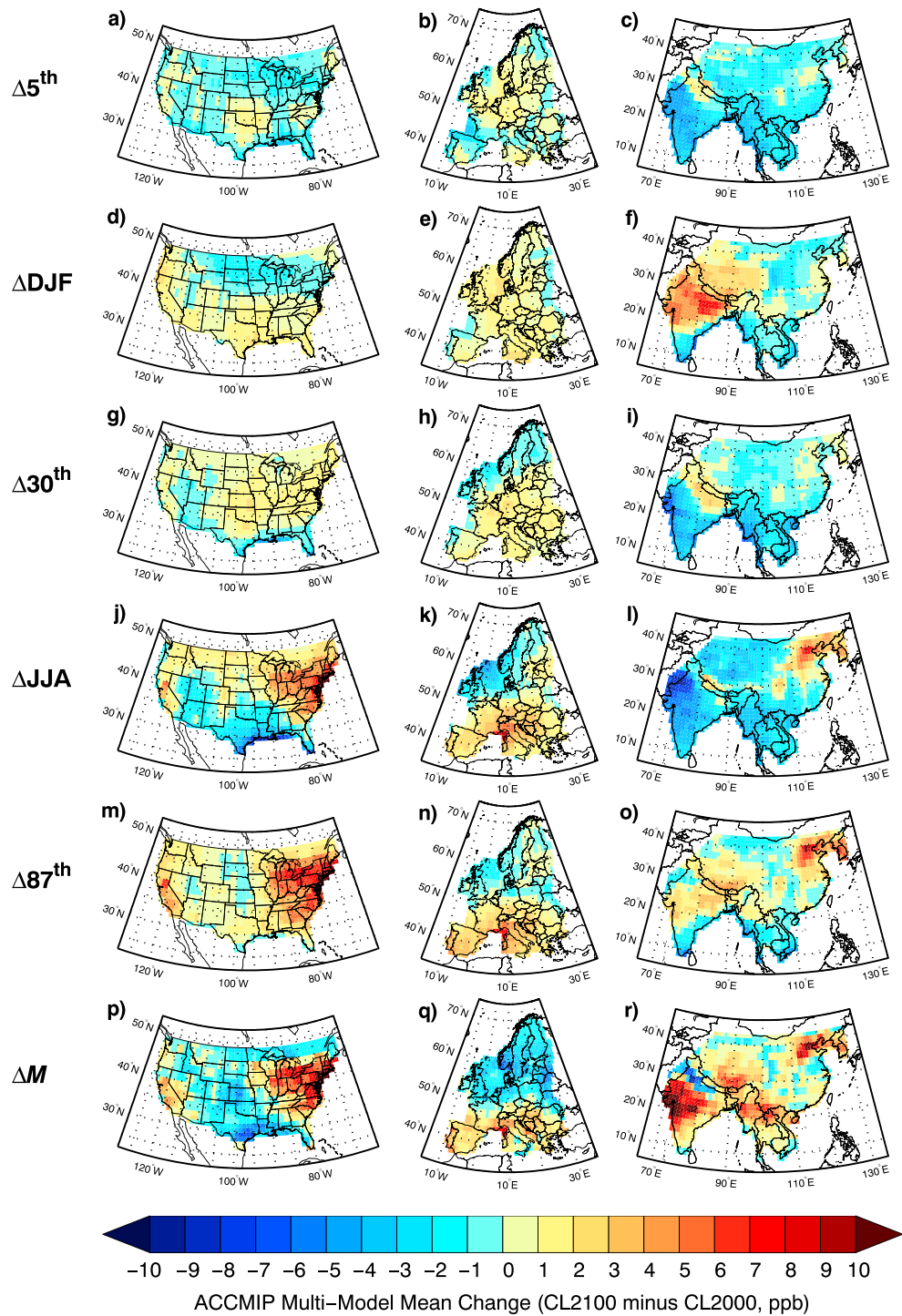
Figure 2. ACCMIP multimodel mean of MDA8 O_3 changes (CL2100 minus CL2000, ppb) in the (a–c) 0–10th percentile bin (Δ5th), (d–f) winter (ΔDJF), (g–i) 30th percentile (Δ30th), (j–k) summer (ΔJJA), (m–o) 87th percentile (Δ87th), and (p–r) peak-to-peak amplitude of the annual cycle (ΔM) over North America (left column), Europe (middle column), and East Asia (right column). Individual model-domain maps for each quantity can be found in the supporting information.

The 30th percentile represents a photochemical baseline O_3 season regardless of seasonal ranking differences; e.g., the lowest O_3 season is not always winter but typically occurs between the 20th and 40th percentiles (Figure 1). The 30th percentile is stable, showing little year-to-year variation in observations and in present-day ACCMIP model simulations (S2015). The multimodel mean of Δ30th over each domain is

shown in Figures 2g–2i, with individual model-domain maps in Figure S6 and model region averages in Table S2. Consistent with ΔDJF, we find positive Δ30th (0 to +3 ppb) over most of NA and EU. Increases are also found over the Himalayan Plateau, likely reflecting increased exchange with the free troposphere or stratosphere [*Hsu et al.*, 2005]. Comparing Δ30th and Δ5th over NA shows that lower O_3 prevails for at least 4 months over the desert southwest and the Gulf Coast. We associate the large negative Δ30th over most of EA (-5 ppb), especially the near-ocean areas, with changes in the Asian summer monsoon since the median percentile of JJA days is within ±5% of the 30th percentile in all models for both CL2000 and CL2100 (Figure 1).

3.2. Changes in High Percentiles and Seasonal Cycle of O_3

The highest surface O_3 abundances typically occur when precursors, sunlight, and meteorology align. Hemispheric-scale processes that alter the basic latitudinal surface O_3 gradients (e.g., the summertime midlatitude jet location [*Barnes and Fiore*, 2013; *Barnes and Polvani*, 2013]) and vertical mixing also play important roles.

The seasons with the highest median percentile are summer (JJA) for ENA and SEU; spring (March-April-May, MAM) for WNA, NEU, and NEA; and either DJF or MAM for SEA (Figure 1). We calculate the timing of peak O_3 (m, days of the year) from the phase of a cosine fit to each grid cell's monthly averaged MDA8 O_3. The seasonal amplitude M (ppb) is also derived from this fit. To see the representativeness of these fits, see S2015 (Figures 1i–1l). Individual model-domain maps of Δm are shown in Figure S7 with model region averages in Table S3.

GFDL-AM3 and UM-CAM show $\Delta m < 0$ (i.e., peak O_3 shifting earlier) in all regions, consistent with an earlier study using transient simulations of the fully coupled GFDL-CM3 over the eastern U.S. [*Clifton et al.*, 2014]. However, *Clifton et al.* [2014] find that the climate impact reinforces the potentially much larger impact of RCP8.5 O_3 precursor emission reductions, particularly with regard to the phase of the seasonal cycle. The largest negative Δm (~15 days) are found over regions where the peak O_3 season is early (MAM), while the smallest are found over JJA peak regions. An earlier arrival of peak O_3 indicates a climate-driven O_3 increase in spring, a decrease in summer, or both. Among the four models, GFDL-AM3 has the largest negative Δm and the largest positive ΔMAM. Overall, 14 of 24 model regions have positive ΔMAM and 17 have negative ΔJJA (Table S2). GISS-E2-R shows later arrivals of peak O_3 ($\Delta m > 0$) in NA and EU regions, possibly related to its climate-sensitive BVOCs, but it also had the poorest simulation of present-day seasonality over WNA and NEU (S2015), thought to be related to excessive wintertime stratosphere-troposphere exchange [*Shindell et al.*, 2013]. MOCAGE also has $\Delta m > 0$ for all regions except WNA (Table S3); however, MOCAGE has $\Delta m < 0$ over most of NA, India, and western China (Figure S7).

GISS-E2-R accounts for five of the seven model regions with positive ΔJJA, almost certainly due to its climate-sensitive BVOCs. Indeed, its largest ΔJJA are in regions with large BVOC emissions: ENA (+7.1 ppb) and SEU (+9.3 ppb). Figures 2j–2l show the multimodel mean of ΔJJA over each domain, with individual model-domain maps in Figure S8 and model region averages in Table S2. We find negative ΔJJA over most of southern NA, northwest EU, and all of EA except northeast China. Negative ΔJJA in the near-ocean areas reflects decreases in boundary O_3. Only GISS-E2-R has positive ΔJJA in these areas because it has increases in boundary O_3. Positive ΔJJA is found over the western and northern edge of NA, the Ohio River Valley extending to the northeast, all of SEU, and northeastern China. These multimodel mean increases largely reflect GISS-E2-R; however, all models show positive ΔJJA over polluted regions such as northeastern NA, the Po Valley, and northeastern China.

Overall, during the peak photochemical season JJA, climate change increases O_3 in polluted regions and decreases O_3 in nearby cleaner regions, broadly consistent with previous findings [e.g., *Johnson et al.*, 1999; *Wu et al.*, 2008]. We hypothesize that warmer temperatures increase the efficiency of precursors to produce O_3 in polluted regions, consequently reducing precursor availability in neighboring, cleaner, downwind locations, where NO_x is usually more efficient in producing O_3. On a much broader scale, *Doherty et al.* [2013] use one model to show that the more rapid thermal decomposition of organonitrates expected in a warming climate can lead to a few ppb increase in the annual average of surface O_3 over land and a corresponding decrease over the oceans. The ACCMIP models used here include all climate-driven effects on photochemical kinetics, and we find that this climate-driven shift in surface O_3 has a much greater magnitude (up to 10 ppb),

is found particularly at higher percentiles of O_3 (i.e., the AQX episodes; see section 3.3), and occurs on the 200 km scale within the continents.

The negative ΔJJA in south central NA and large positive ΔJJA over the northeast may indicate a CL2100 westward extension of the Bermuda High and subsequent changes in the related Great Plains low-level jet [e.g., *Eder et al.*, 1993; *Fiore et al.*, 2003; *Shen et al.*, 2015]. Some studies suggest an ~5° westward shift in this pattern by 2100 [*Li et al.*, 2012, 2013], which would decrease O_3 in central NA through enhanced flux of low-O_3 air from the Gulf of Mexico but increase O_3 in northeast NA by extending the high-pressure system's stagnant conditions. This pattern is seen in all four models (Figures S8a, S8d, S8g, and S8j) but at different magnitudes.

The 87th percentile was chosen in S2015 to represent the median value of a hypothetical season containing all high-O_3 days. It allows for peak O_3 to shift away from JJA and thus is a more robust measure of the photochemical O_3 season. The multimodel mean of Δ87th over each domain is shown in Figures 2m–2o, with individual model-domain maps in Figure S9 and model region averages in Table S2. We find Δ87th is predominantly positive and largest over the most polluted regions (e.g., California, ENA, SEU, and northeast China). This feature is largely consistent with ΔJJA patterns, but it is more pronounced and missing the JJA reductions due to CL2100-enhanced onshore flow in south central NA and the monsoon regions of EA.

The amplitude of the O_3 annual cycle increases with climate change: 17 of 24 model regions show positive ΔM (Figures 2p–2r and S10 and Table S3). Like Δ87th and ΔJJA, the largest positive ΔM are found in the most polluted regions whereas the largest negative ΔM are found in southern NA and northern EU (where ΔJJA is most negative). The mostly positive ΔM may appear contradictory to general findings of negative ΔJJA and positive ΔDJF but instead indicates a shift in peak O_3 away from JJA and in the lowest O_3 away from DJF. The geographic patterns of ΔM, ΔJJA, and Δ87th coincide roughly with areas where the proxy index for stagnation days changes in a future climate [*Horton et al.*, 2014].

3.3. Changes in Air Quality Extreme (AQX) Episodes

Air quality extreme (AQX) *events* are defined for each grid cell as the 10 times N worst days (i.e., highest MDA8) in an N year period [see *Schnell et al.*, 2014]. Because AQX events are defined as a return time, we cannot evaluate climate-driven changes in the number of events; however, we can quantify shifts in their relative intensity, seasonality, and the space-time clustering of events into episodes.

We evaluate AQX seasonality by deriving the timing of maximum phase (m_{AQX}, days of the year) from a cosine fit to each grid cell's monthly binned AQX events. With climate change, AQX events generally shift to earlier in the year ($\Delta m_{AQX} < 0$ for 16 of 24 model regions), by a greater amount than the seasonal cycle of MDA8 (Table S3). Because of its climate-driven BVOC emissions, GISS-E2-R has more AQX events in late summer and positive Δm_{AQX} for NA and EU, consistent with its large ΔJJA.

Neighboring AQX events connected in space and/or time are clustered into AQX *episodes* [*Schnell et al.*, 2014]. Episode sizes S range from a single-cell, 1 day event (~10^4 km^2 d) to multiday episodes spanning hundreds of kilometers (>1000×10^4 km^2 d). For each model region, we calculate (i) a complementary cumulative distribution of episodes as a function of size (CCD_S, percent of events' areas in episodes of size S or larger); (ii) a mean episode size ($\langle S \rangle$, 10^4 km^2 d, weighted geometric mean with weights equal to S [*Schnell et al.*, 2014, equation 6]); (iii) an episode enhancement as a function of size (E_S, ppb, time-area weighted average of the magnitude of all AQX event cells above each cell's 30th percentile O_3 value); and (iv) the average enhancement increase with episode size ($\partial E_S / \partial S$, ppb/decade) for episodes $S \geq 30 \times 10^4$ km^2 d (S2015). Climate-driven changes have different units: (i) ΔCCD_S as absolute differences in CCD_S (%, Figures 3a–3f); (ii) $\Delta\langle S \rangle$ as percent relative to CL2000 to account for the large intermodel and interregion range of episode sizes (Table S4); and (iii) ΔE_S as a 2-D color-contour plot of the multimodel mean percent change in E_S (designated by the color bar) as a function of enhancement for each log-scale size bin in S (Figures 3g–3l). For each half-decade size bin (edges at 3, 10, 30, 100, 300, 1000, and >1000×10^4 km^2 d), the sum of ΔE_S is zero; a red color indicates where particular enhancements E_S are relatively more prevalent, and a blue color, where less prevalent.

Figures 3a–3f show ΔCCD_S for each model region plotted at each half decade in S. As expected, the largest ΔCCD_S is found for $S > 300 \times 10^4$ km^2 d where the CCD_S curve is steepest (S2015), but the sign is often split between the models in each region. The models are similarly split for $\Delta\langle S \rangle$, with 11 of 24 model regions showing positive values (Table S4). The sign of $\Delta\langle S \rangle$ and ΔCCD_S for the largest S generally match for each model region.
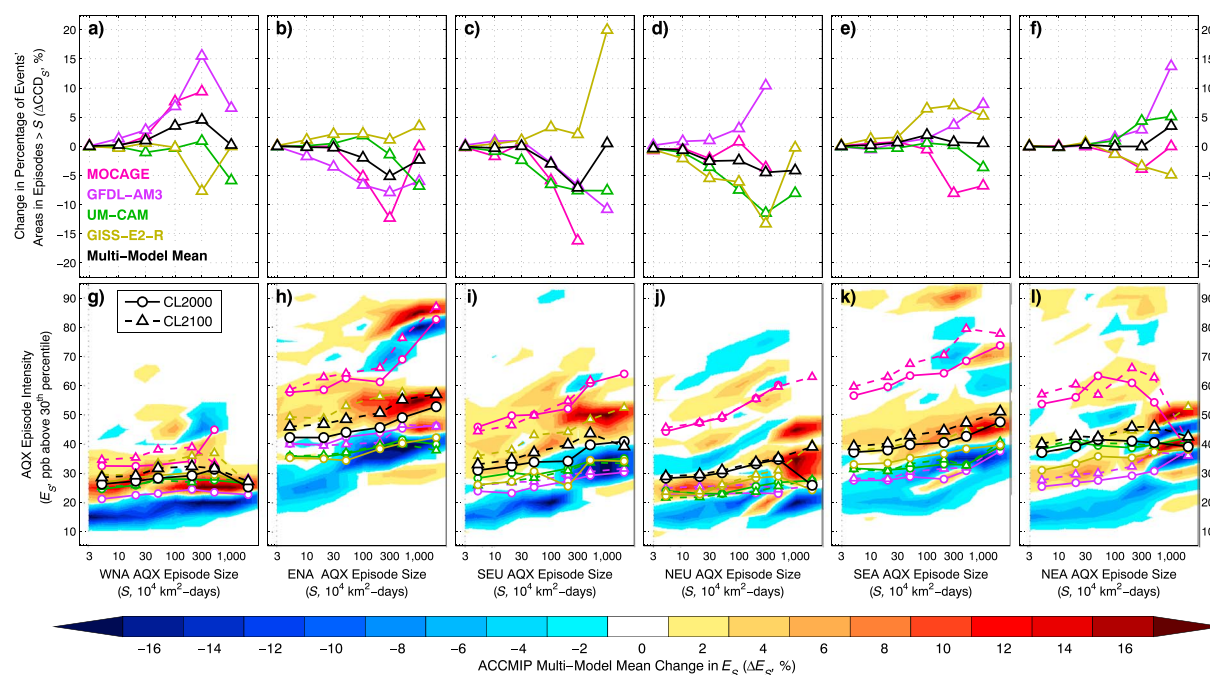
Figure 3. (a–f) Change in the complementary cumulative distribution (ΔCCD_S, %) of the percentage of total areal extent of all individual AQX events plotted at the endpoints of each half decade in AQX episode size (S, 10^4 km^2 d) for each ACCMIP model (colors) and the multimodel mean (black). (g-l) Density contour of the ACCMIP multimodel mean change in AQX episode enhancement E_S versus S (ΔE_S, %, colors corresponding to the color bar). The overlain curves show the mean area-weighted enhancement E_S (ppb above the 30th percentile) of each size bin for CL2000 (solid line, open circles) and CL2100 (dashed lines, open triangle) for each ACCMIP model (colors) and the multimodel mean (black). Columns from left to right correspond to regions: WNA, ENA, SEU, NEU, SEA, and NEA.

These mixed results provide little confidence in how the distribution of sizes or mean size of future AQX episodes will change. Yet for the very largest episodes there is some consensus: 17 of 24 model regions, and at least two models in each region, show increases in the average size of the largest two episodes (Table S4).

The mean value of E_S averaged over each size bin is shown for each model and the multimodel mean for CL2000 (circles) and CL2100 (triangles) in Figures 3g–3l. In all regions except NEU (the least photochemically active), CL2100 episodes show greater enhancements, particularly for $S > 100 \times 10^4$ km^2 d. The color-contour plot of multimodel mean ΔE_S supports this, clearly showing that the largest enhancements (those above the mean) are more common, while those below are less common. The change in the average episode enhancement ($\Delta \langle E_S \rangle$, ppb) is positive in 17 of 24 model regions (Table S4). This finding is consistent with increased seasonal amplitudes ($\Delta M > 0$), and all model regions with positive ΔM have positive $\Delta \langle E_S \rangle$.

Prior analysis of NA and EU observations shows that larger episodes have on average larger enhancements, with a slope $\partial E_S / \partial S$ of 2 to 4 ppb/decade (S2015) that most models can reproduce. For CL2100, the slope becomes steeper, and $\Delta(\partial E_S / \partial S) > 0$ in 14 of the 24 model regions (Table S4).

4. Summary and Conclusions

We investigate the effect of climate change on MDA8 surface O$_3$ over North America, Europe, and East Asia using four global models that participated in ACCMIP and archived hourly surface ozone abundances. We use climate change projected from scenario CL2000 (decade of the 2000s) to CL2100 (first decade of the 2100 s, high-CO$_2$ RCP8.5 scenario with global mean temperature increase of ~4°C) and fixed anthropogenic O$_3$ precursor emissions (and methane concentrations for chemistry) for CL2000 and CL2100. We focus on North America and Europe for which present-day observations can be used to test the models (see S2015) and on East Asia, which consists of the midlatitude northern part and the monsoonal southern part.

Overall, the diverse patterns of O$_3$ change among the four models, plus the large climate-driven changes in BVOCs in one model, make it difficult to present a simple plot of future O$_3$ (even with fixed anthropogenic emissions). We present individual model as well as multimodel mean results but feel that the model mean

plots cover up current modeling uncertainty in this simulation. Nevertheless, we find some consistencies that we believe will survive a more thorough assessment. Climate change shifts the timing of peak O_3 to earlier in the year and increases the amplitude of the annual cycle. Similarly, climate change spreads out and shifts the timing of air quality extreme (AQX) events to earlier in the year. There are clear seasonal differences in baseline O_3 levels entering the continents for CL2100, but the cause is unclear.

Increases in summertime mean and high-percentile O_3 are generally found in polluted environments, with decreases found in clean environments. We propose that this pattern of "the most polluted get worse while their neighbors get better" reflects an augmented efficiency of precursor emissions to generate surface O_3 in the polluted regions under future climate change (warmer temperatures, more water vapor, and faster chemical kinetics), thus reducing export of precursors to neighboring downwind locations. All models show climate-driven increases in summertime surface O_3 over the northeast U.S., the Po Valley, and northeast China. Even with constant biogenic emissions, climate change increases O_3 at the upper tail of the probability distribution in most models and regions. In most cases, AQX episodes become larger and contain higher O_3 levels relative to the rest of the distribution. Thus, the extremes become more hazardous.

Further studies of the climate-driven changes in air quality, as opposed to local emissions-driven changes, should include a wider range of models and assess the balance between changes in anthropogenic and natural emissions of O_3 precursors. Broader chemistry-climate model participation is needed to develop more robust findings. Including models with more ensemble members and simulation years may further reduce the uncertainty of climate change impacts on O_3 and related photochemistry. Nevertheless, the indication here that the most extreme air pollution episodes are more likely than not to become more extensive and more severe poses a serious challenge for our posterity in managing air quality.

References

Ainsworth, E. A., and A. Rogers (2007), The response of photosynthesis and stomatal conductance to rising [CO_2]: Mechanisms and environmental interactions, *Plant Cell Environ.*, *30*, 258–270, doi:10.1111/j.1365-3040.2007.01641.x.

Barnes, E. A., and A. M. Fiore (2013), Surface ozone variability and the jet position: Implications for projecting future air quality, *Geophys. Res. Lett.*, *40*, 2839–2844, doi:10.1002/grl.50411.

Barnes, E. A., and L. Polvani (2013), Response of the midlatitude jets, and of their variability, to increased greenhouse gases in the CMIP5 models, *J. Clim.*, *26*(18), 7117–7135, doi:10.1175/jcli-d-12-00536.1.

Camalier, L., W. Cox, and P. Dolwick (2007), The effects of meteorology on ozone in urban areas and their use in assessing ozone trends, *Atmos. Environ.*, *41*(33), 7127–7137, doi:10.1016/j.atmosenv.2007.04.061.

Christensen, J. H., et al. (2013), Chapter 14, climate phenomena and their relevance for future regional climate change, in *Climate Change 2013: The Physical Science Basis. Contribution of Working Group I to the Fifth Assessment Report of the Intergovernmental Panel on Climate Change*, edited by T. F. Stocker et al., Cambridge Univ. Press, Cambridge, U. K.

Clifton, O. E., A. M. Fiore, G. Correa, L. W. Horowitz, and V. Naik (2014), Twenty-first century reversal of the surface ozone seasonal cycle over the northeastern United States, *Geophys. Res. Lett.*, *41*, 7343–7350, doi:10.1002/2014GL061378.

Cubasch, U., D. Wuebbles, D. Chen, M. C. Facchini, D. Frame, N. Mahowald, and J.-G. Winther (2013), Introduction, in *Climate Change 2013: The Physical Science Basis. Contribution of Working Group I to the Fifth Assessment Report of the Intergovernmental Panel on Climate Change*, edited by T. F. Stocker et al., Cambridge Univ. Press, Cambridge, U. K., and New York.

Doherty, R. M., et al. (2013), Impacts of climate change on surface ozone and intercontinental ozone pollution: A multi-model study, *J. Geophys. Res. Atmos.*, *118*, 3744–3763, doi:10.1002/jgrd.50266.

Eder, B. K., J. M. Davis, and P. Bloomfield (1993), A characterization of the spatiotemporal variability of nonurban ozone concentrations over the eastern United States, *Atmos. Environ. Part A*, *27*(16), 2645–2668, doi:10.1016/0960-1686(93)90035-w.

Fiore, A. M., D. J. Jacob, R. Mathur, and R. V. Martin (2003), Application of empirical orthogonal functions to evaluate ozone simulations with regional and global models, *J. Geophys. Res.*, *108*(D19), 4431, doi:10.1029/2002JD003151.

Fiore, A. M., et al. (2012), Global air quality and climate, *Chem. Soc. Rev.*, *41*(19), 6663–6683, doi:10.1039/c2cs35095e.

Fiore, A. M., V. Naik, and E. M. Leibensperger (2015), Air quality and climate connections, *J. Air Waste Manage. Assoc.*, *65*(6), 645–685, doi:10.1080/10962247.2015.1040526.

Guenther, A., et al. (1995), A global model of natural volatile organic compound emissions, *J. Geophys. Res.*, *100*(D5), 8873–8892, doi:10.1029/94JD02950.

Heald, C., M. J. Wilkinson, R. K. Monson, C. A. Alos, G. Wang, and A. Guenther (2009), Response of isoprene emission to ambient CO_2 changes and implications for global budgets, *Global Change Biol.*, *15*(5), 1127–1140, doi:10.1111/j.1365-2486.2008.01802.x.

Hogrefe, C., B. Lynn, K. Civerolo, J. Ku, J. Rosenthal, C. Rosenzweig, R. Goldberg, S. Gaffin, K. Knowlton, and P. Kinney (2004), Simulating changes in regional air pollution over the eastern United States due to changes in global and regional climate and emissions, *J. Geophys. Res.*, *109*, D22301, doi:10.1029/2004JD004690.

Holloway, T., S. N. Spak, D. Barker, M. Bretl, C. Moberg, K. Hayhoe, J. Van Dorn, and D. Wuebbles (2008), Change in ozone air pollution over Chicago associated with global climate change, *J. Geophys. Res.*, *113*, D22306, doi:10.1029/2007JD009775.

Horton, D. E., C. B. Skinner, D. Singh, and N. S. Diffenbaugh (2014), Occurrence and persistence of future atmospheric stagnation events, *Nat. Clim. Change*, *4*(8), 698–703, doi:10.1038/nclimate2272.

Hsu, J., M. J. Prather, and O. Wild (2005), Diagnosing the stratosphere-to-troposphere flux of ozone in a chemistry transport model, *J. Geophys. Res.*, *110*, D19305, doi:10.1029/2005JD006045.

Jacob, D. J., and D. A. Winner (2009), Effect of climate change on air quality, *Atmos. Environ.*, *43*(1), 51–63, doi:10.1016/j.atmosenv.2008.09.051.

Johnson, C. E., W. J. Collins, D. S. Stevenson, and R. G. Derwent (1999), Relative roles of climate and emissions changes on future tropospheric oxidant concentrations, *J. Geophys. Res.*, *104*(D15), 18,631–18,645, doi:10.1029/1999JD900204.

Kirtman, B., et al. (2013), Near-term climate change: Projections and predictability, in *Climate Change 2013: The Physical Science Basis. Contribution of Working Group I to the Fifth Assessment Report of the Intergovernmental Panel on Climate Change*, edited by T. F. Stocker et al., Cambridge Univ. Press, Cambridge, U. K., and New York.

Lamarque, J. F., et al. (2013), The Atmospheric Chemistry and Climate Model Intercomparison Project (ACCMIP): Overview and description of models, simulations and climate diagnostics, *Geosci. Model Dev.*, *6*(1), 179–206, doi:10.5194/gmd-6-179-2013.

Leibensperger, E., L. Mickley, and D. Jacob (2008), Sensitivity of US air quality to mid-latitude cyclone frequency and implications of 1980–2006 climate change, *Atmos. Chem. Phys.*, *8*(23), 7075–7086, doi:10.5194/acp-8-7075-2008.

Li, L., W. Li, and Y. Deng (2013), Summer rainfall variability over the Southeastern United States and its intensification in the 21st century as assessed by CMIP5 models, *J. Geophys. Res. Atmos*, *118*, 340–354, doi:10.1002/jgrd.50136.

Li, W., L. Li, M. Ting, and Y. M. Liu (2012), Intensification of Northern Hemisphere subtropical highs in a warming climate, *Nat. Geosci.*, *5*(11), 830–834, doi:10.1038/ngeo1590.

Lin, J. T., K. O. Patten, K. Hayhoe, X. Z. Liang, and D. J. Wuebbles (2008), Effects of future climate and biogenic emissions changes on surface ozone over the United States and China, *J. Appl. Meteorol. Climatol.*, *47*(7), 1888–1909, doi:10.1175/2007jamc1681.1.

Logan, J. A. (1989), Ozone in rural areas of the United States, *J. Geophys. Res.*, *94*(D6), 8511–8532, doi:10.1029/JD094iD06p08511.

Mahmud, A., M. Tyree, D. Cayan, N. Motallebi, and M. J. Kleeman (2008), Statistical downscaling of climate change impacts on ozone concentrations in California, *J. Geophys. Res.*, *113*, D21103, doi:10.1029/2007JD009534.

Mickley, L., D. Jacob, B. Field, and D. Rind (2004), Effects of future climate change on regional air pollution episodes in the United States, *Geophys. Res. Lett.*, *31*, L24103, doi:10.1029/2004GL021216.

Myhre, G., et al. (2013), Anthropogenic and natural radiative forcing, in *Climate Change 2013: The Physical Science Basis. Contribution of Working Group I to the Fifth Assessment Report of the Intergovernmental Panel on Climate Change*, edited by T. F. Stocker et al., Cambridge Univ. Press, Cambridge, U. K., and New York.

Naik, V., L. W. Horowitz, A. M. Fiore, P. Ginoux, J. Mao, A. M. Aghedo, and H. Levy II (2013), Impact of preindustrial to present-day changes in short-lived pollutant emissions on atmospheric composition and climate forcing, *J. Geophys. Res. Atmos.*, *118*, 8086–8110, doi:10.1002/jgrd.50608.

Ordonez, C., H. Mathis, M. Furger, S. Henne, C. Huglin, J. Staehelin, and A. S. H. Prevot (2005), Changes of daily surface ozone maxima in Switzerland in all seasons from 1992 to 2002 and discussion of summer 2003, *Atmos. Chem. Phys.*, *5*, 1187–1203, doi:10.5194/acp-5-1187-2005.

Pfister, G. G., S. Walters, J.-F. Lamarque, J. Fast, M. C. Barth, J. Wong, J. Done, G. Holland, and C. L. Bruyère (2014), Projections of future summertime ozone over the U.S, *J. Geophys. Res. Atmos.*, *119*, 5559–5582, doi:10.1002/2013JD020932.

Rieder, H. E., A. M. Fiore, L. W. Horowitz, and V. Naik (2015), Projecting policy-relevant metrics for high summertime ozone pollution events over the eastern United States due to climate and emission changes during the 21st century, *J. Geophys. Res. Atmos*, *120*, 784–800, doi:10.1002/2014JD022303.

Schnell, J. L., C. D. Holmes, A. Jangam, and M. J. Prather (2014), Skill in forecasting extreme ozone pollution episodes with a global atmospheric chemistry model, *Atmos. Chem. Phys.*, *14*(15), 7721–7739, doi:10.5194/acp-14-7721-2014.

Schnell, J. L., et al. (2015), Use of North American and European air quality networks to evaluate global chemistry-climate modeling of surface ozone, *Atmos. Chem. Phys.*, *15*(18), 10,581–10,596, doi:10.5194/acp-15-10581-2015.

Shen, L., L. J. Mickley, and A. P. K. Tai (2015), Influence of synoptic patterns on surface ozone variability over the eastern United States from 1980 to 2012, *Atmos. Chem. Phys.*, *15*(19), 10,925–10,938, doi:10.5194/acp-15-10925-2015.

Shindell, D. T., et al. (2013), Interactive ozone and methane chemistry in GISS-E2 historical and future climate simulations, *Atmos. Chem. Phys.*, *13*(5), 2653–2689, doi:10.5194/acp-13-2653-2013.

Stevenson, D. S., et al. (2013), Tropospheric ozone changes, radiative forcing and attribution to emissions in the Atmospheric Chemistry and Climate Model Intercomparison Project (ACCMIP), *Atmos. Chem. Phys.*, *13*(6), 3063–3085, doi:10.5194/acp-13-3063-2013.

Thambiran, T., and R. D. Diab (2010), A review of scientific linkages and interactions between climate change and air quality, with implications for air quality management in South Africa, *S. Afr. J. Sci.*, *106*(3–4), 20–27, doi:10.4102/sajs.v106i3/4.56.

Voulgarakis, A., et al. (2013), Analysis of present day and future OH and methane lifetime in the ACCMIP simulations, *Atmos. Chem. Phys.*, *13*(5), 2563–2587, doi:10.5194/acp-13-2563-2013.

Wu, S. L., L. J. Mickley, E. M. Leibensperger, D. J. Jacob, D. Rind, and D. G. Streets (2008), Effects of 2000–2050 global change on ozone air quality in the United States, *J. Geophys. Res.*, *113*, D06302, doi:10.1029/2007JD008917.

Young, P. J., et al. (2013), Pre-industrial to end 21st century projections of tropospheric ozone from the Atmospheric Chemistry and Climate Model Intercomparison Project (ACCMIP), *Atmos. Chem. Phys.*, *13*(4), 2063–2090, doi:10.5194/acp-13-2063-2013.

Zeng, G., and J. A. Pyle (2003), Changes in tropospheric ozone between 2000 and 2100 modeled in a chemistry-climate model, *Geophys. Res. Lett.*, *30*(7), 1392, doi:10.1029/2002GL016708.